Journal of Power Sources 278 (2015) 473–483

Contents lists available at ScienceDirect

Journal of Power Sources

journal homepage: www.elsevier.com/locate/jpowsour

Capacity and power fade cycle-life model for plug-in hybrid electric vehicle lithium-ion battery cells containing blended spinel and layered-oxide positive electrodes

Andrea Cordoba-Arenas [a, *], Simona Onori [b, 1], Yann Guezennec [a], Giorgio Rizzoni [a]

[a] Center for Automotive Research and Department of Mechanical and Aerospace Engineering, The Ohio State University, Columbus, OH 43212, USA
[b] Department of Automotive Engineering, Clemson University, Greenville 29607, USA

HIGHLIGHTS

- Capacity and power fade aging model for lithium-ion cells containing NMC-LMO cathodes.
- Control-oriented cycle-life model for PHEV applications.
- Understanding of lithium-ion battery aging under realistic PHEV operation.

ARTICLE INFO

Article history:
Received 25 August 2014
Received in revised form
20 November 2014
Accepted 13 December 2014
Available online 15 December 2014

Keywords:
Lithium-ion battery
Capacity and power fade
NMC-LMO cathode
Semi-empirical model
Cycle-life prognosis
PHEV cycling

ABSTRACT

This paper proposes and validates a semi-empirical cycle-life model for lithium-ion pouch cells containing blended spinel and layered-oxide positive electrodes. For the model development and validation experimental data obtained during an aging campaign is used. During the campaign the influence of charge sustaining/depleting operation, minimum state of charge (SOC), charging rate and temperature on the aging process is studied. The aging profiles, which are prescribed in power mode, are selected to be representative of realistic plug-in hybrid electric vehicle (PHEV) operation. The proposed model describes capacity fade and resistance increase as function of the influencing stress factors and battery charge throughput. Due to its simplicity but still good accuracy, the applications of the proposed aging model include the design of algorithms for battery state-of-health (SOH) monitoring and prognosis, PHEV optimal energy management including battery aging, and the study of aging propagation among battery cells in advanced energy storage systems.

1. Introduction

A crucial step towards the large-scale introduction of plug-in hybrid electric vehicles (PHEVs) in the market is to reduce the cost of their energy storage devices. Lithium-ion (Li-ion) batteries are the preferred energy storage technology in PHEVs due to their high energy and power density [1]. One of the goals of U.S Department of Energy (DOE) Vehicle Technologies Program for hybrid electric systems is to, by 2022, reduce the production cost of Li-ion batteries by nearly 75% from 2012 costs. Currently, battery cycle and calendar life represents one of the greatest uncertainties in the total life-cycle cost of advanced energy storage systems [2].

Generally, battery aging manifest itself in a reduction in the ability to store energy and deliver power, performance metrics correlated with loss in capacity and increase in internal resistance [3,4]. Among the micro-mechanisms of Li-ion battery aging we cite active particle loss and metal sediment or SEI film accumulation. A review of today' s knowledge on the mechanics of aging in Li-ion batteries can be found in Refs. [3,5]. These physical-chemical mechanisms are enhanced by stress factors such as current severity (C-rate), operating temperature, state of charge (SOC), cycling rates, overcharge and over-discharge [3,4]. The generation of long-term predictions of the evolution of capacity and/or resistance to predict when it will reach a predetermined threshold is referred as battery prognosis. Prognosis helps in making informed

* Corresponding author.
E-mail addresses: cordoba-arenas.1@osu.edu (A. Cordoba-Arenas), sonori@clemson.edu (S. Onori), guezennec.1@osu.edu (Y. Guezennec), rizzoni.1@osu.edu (G. Rizzoni).

[1] Part of this research was conducted at the time Dr. Onori was Research Scientist at OSU-CAR.

http://dx.doi.org/10.1016/j.jpowsour.2014.12.047
0378-7753/

and timely life cycle management decisions, reducing warranty and maintenance costs while improving serviceability, availability and safety. Prognosis is possible when an aging model describing the evolution of aging over time/cycle is available.

Battery aging models can be classified as physics-based [6–13] and semi-empirical models [2,14]. Due to its simplicity but still good accuracy, semi-empirical models have been used for on-line battery prognosis and state-of-health (SOH) estimation, and as part of other Battery Management System (BMS) tasks such as state-of-charge (SOC) estimation [4,15]. Recently, semi-empirical models have been also used for PHEV optimal energy management including battery aging [16,17] and for the study of aging propagation among cells in advanced battery systems [18]. Due to its potential applications, in this work, we choose to use the semi-empirical approach for the aging model development.

During the past years, the concept of blended electrodes composed of several active materials is attracting attention. Blended cathodes promise the combination of benefits of different metal-oxides into a hybrid electrode to allow performance optimization [19,20]. In particular, blended cathodes composed of layered-oxide positive electrodes such as $LiNi_{1/3}Nm_{1/3}Co_{1/}\ O_2$ (NMC) and spinel oxide positive electrodes such as $LiMn_2O_4$ (LMO) have been considered as one of the most promising candidates for PHEV applications [21,22]. NMC positive electrodes have high specific capacity, good thermal stability and good cycle life. However, they have poor performance at high rates [21]. On the other hand, LMO positive electrodes, have a high rate capability and a low-cost. However, they have a low cycle life [19]. NMC-LMO blended positive electrodes have been reported to have the benefits of the two metal-oxides [23,21].

There have been substantial efforts to conduct experimental campaigns to understand the influence of different stress factors on battery aging for various cathode materials: $LiCoO_2$ (LCO) [24,25], LiNiO (LNO) [24], $Li(Ni,Co)O_2$ (NCO) [26–29], $Li(Ni,Co,Al)O_2$ (NCA) [30,25,31,32], $LiFePO_4$ (LFP) [2,14,32], NMC [33–35]. The majority of these studies have also included efforts to develop semi-empirical aging models. The main stress factors investigated have been SOC, ΔSOC, C-rate, and Temperature. Recently, other PHEV related stress factors such as vehicle-to-grid services (V2G) [36], charging protocol [37] and SOC equalization [38] have been included.

Though NMC-LMO cathodes are considered an excellent candidate for PHEV applications, only few aging campaigns using this composite material have been published [39–41,13]. In Ref. [39] the effect of temperature and SOC on calendar-life and charge sustaining/depleting cycle-life are studied within a large aging campaign. In Ref. [40], cycle-life is studied under two scenarios. In the first one, the effect of thermal cycling superimposed to charge sustaining/depleting operation is studied. In the second one, the magnitude and randomness of constant power pulses is investigated. None of these studies have included the development of suitable aging models for BMS and prognostics schemes.

Despite the efforts reported in the literature, there is still the need to understand battery aging under more realistic PHEV operation. In particular, the development of accurate aging models able to assess and prognose the life of the most advanced li-ion cathode candidates under realistic automotive scenarios is critical. This paper proposes semi-empirical capacity and power fade aging models for Li-ion pouch cells with NMC-LMO positive electrodes based on PHEV aging cycles. During the aging campaign that provided data for the proposed model, the influence of charge sustaining/depleting operation, minimum SOC, charging rate and temperature on the aging process was studied [13].

This paper is organized as follows. Section 2 describes the design of experiments and the methodology used during the periodic state of health assessments. Sections 3 and 4 present the capacity fade experimental data and describe the development and validation of an aging model based on empirical relations of the stress factors with capacity fade. Sections 5 and 6 present the resistance increase experimental data and describe the development and validation of a power fade model. In Section 7, the conclusions are presented.

2. Experimental campaign

The United States Advanced Battery Consortium (USABC) defines two operational modes for PHEVs, Charge-Depleting (CD) and Charge-Sustaining (CS) [1]. In CD mode the vehicle is allowed to operate in electric mode (i.e. the vehicle powered by the electric drive and onboard electric energy storage) and hybrid mode (i.e. the vehicle is powered by the electric drive and/or engine), with a net decrease in battery state-of-charge (SOC). Where the battery SOC is defined as the available capacity expressed as a percentage of rated capacity. In CS mode the vehicle is only allowed to operate in hybrid mode with a relatively constant battery SOC. Fig. 1 shows an schematic of a typical SOC profile under PHEV cycle operation. During CD the battery is depleted starting from a battery SOC of SOC_{max} and until reaching a predefined SOC_{min}. During CS the battery SOC is kept within a window UE_{CS} with an average value of SOC_{min} [1], see Fig. 1. We define t_{CD} as the time spent in CD, t_{CS} as the time spent in CS, and $(t_{CD} + t_{CS})$ as the total operating time. The ratio of CD to the total operating time is then defined as the ratio of t_{CD} to $(t_{CD} + t_{CS})$,

$$Ratio = \left(t_{CD} : \left(t_{CD} + t_{CS}\right)\right) = \frac{t_{CD}}{t_{CD} + t_{CS}} \tag{1}$$

which indicates the fraction of time spent in CD mode over the total operation time. Therefore, $Ratio = 1$ corresponds to CD operation i.e. all the operating time is spent in CD. $Ratio = 0$ corresponds to CS operation, i.e all the operating time is spent in CS. *Ratios* such that $0 < Ratio < 1$ correspond to mixed operation i.e. the total operating time is divided between CD and CS. For example, the SOC profile shown in Fig. 1 corresponds to mixed operation with a *Ratio* of 1/2, i.e, half of the CD-CS operation time is spent in CD while the other half is spent in CS.

Battery charging is typically done through CC-CV protocol [37]. That is, a constant current (CC) is used until the battery voltage reaches a predetermined limit, followed by a constant voltage (CV) until the current declines to a predetermined value. In this work we

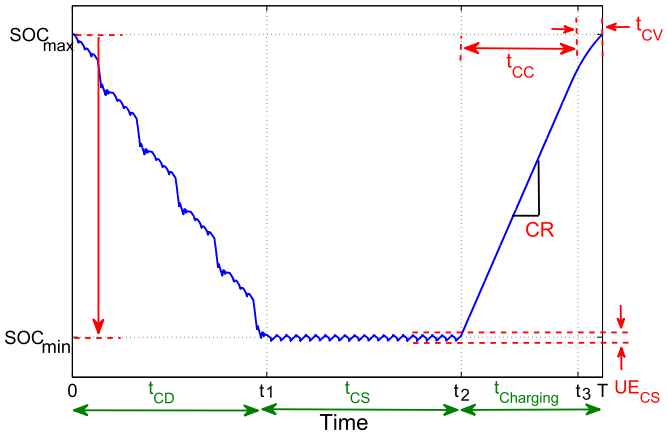

Fig. 1. Schematic of SOC profile under PHEV operation: charge depleting (CD), charge sustaining (CS) and charging.

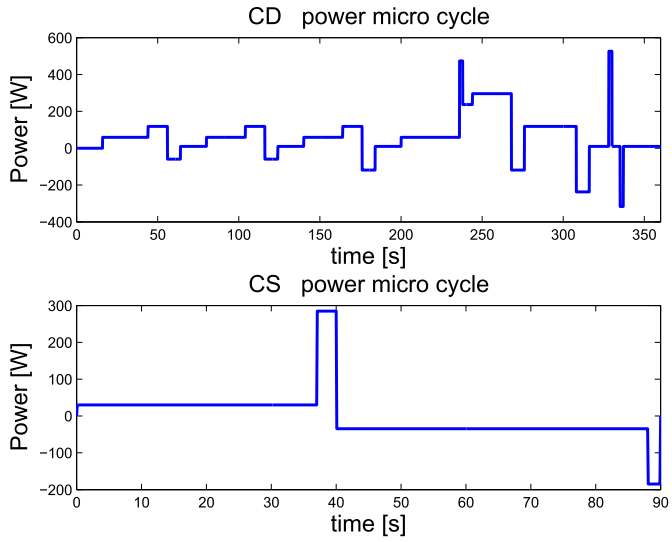

Fig. 2. Charge depliting (CD) and charge sustaining (CD) power micro-cycles.[1].

express the current in terms of C-rate.[2] We refer to the CC expressed in C-rate as charging rate (CR).

2.1. Design of experiments

In order to understand battery aging under a more realistic vehicle cycle-life scenario; in this work, the following stress factors are defined for PHEV operation:

- Charging rate, CR
- Battery skin temperature, T
- t_{CD} to $(t_{CD} + t_{CS})$ *Ratio*
- Minimum state-of-charge, SOC_{min}

To understand the dependence of aging on the stress factors, the experimental data obtained during an aging campaign conducted on pouch cells with composite NMC-LMO positive electrode and carbon graphite negative electrode is used.[3] The design of experiments, previously reported in Ref. [13], is summarized in this section. Each cell has a nominal capacity of 15 Ah at 1C-rate and a nominal voltage of 3.75 V. The battery cell cycling equipment consisted on 400 channels with a maximum capability of 8 V charge, 5 V discharge and 400 A, controlled using Labview.

The duty cycles used during the aging campaign are composed of the PHEV CD and CS micro-cycles defined by the USABC [1]. The duty cycles are prescribed in power mode, not current mode, preserving vehicle performance regardless of SOC and Temperature. In Fig. 2 the power micro-cycles, which are scaled up to approximate a ten-mile CD range PHEV using a BSF[4] of 94, are shown.

Three sets of experiments were conducted:

- One set for CD operation, i.e. *Ratio* = 1
- One set for CS operation, i.e. *Ratio* = 0
- One set for mixed operation, i.e. 0 < *Ratio* < 1

For the CD operation experiment, the power duty cycle consists of either five, six, or seven times a CD micro-cycle to cause an SOC_{min} of approximately 45, 35, or 25%, respectively. Then the cell is charged using a CR of C/3, 3C/2, or 5C to a voltage of 4.15 V, where a CV portion finishes the charge to 95% SOC and the entire cycle is repeated. A total of 9 CD experiments, one for each case, were conducted at 30 °C.

For the CS experiment, the SOC is set by using the cell OCV vs. SOC curve to select the voltage corresponding to an SOC_{min} of 45%, 35% or 25%, respectively, then a CS micro cycle is repeated while keeping the voltage within a window of 10 mV around the nominal setpoint. A total of 3 CS experiments, one for each case, were conducted at 30 °C.

For the mixed operation experiment, the power duty cycle consists of seven times a CD micro-cycle to cause an SOC_{min} of approximately 35%, followed by CS micro-cycles repeated in *Ratios* of 1/2 and 1/4. Then the cell is charged using a CR of 3C/2 following the protocol previously described and the entire cycle is repeated. Three experiments corresponding to a *Ratio* of 1/2, each one conducted at 10 °C, 30 °C or 45 °C. One experiment corresponding to a ratio of 1/4 was conducted at 30 °C. A total of 4 experiments were conducted.

Table 1 contains the summary of the experiments during the aging campaign. The campaign duration was up to 3 months of effective cycling test time. The resulting charge throughput expressed in ampere-hour throughput (Ah) attained at the end of each experiment is shown in the last column of the table.

2.2. Cell characterization

Prior to and after the aging campaign, each cell was characterized using the following tests:

- Capacity test;
- Hybrid Power Pulse Characterization (HPPC).[5] Test used to assess discharge and regen power capability

For the capacity test, the cell was fully charged and then discharge using a constant current of 1C (15 A) to the lower voltage limit. The voltage limits used during the test were $V_{max} = 4.14$ V and $V_{min} = 2.8$ V. The capacity was measured 3 times to establishe repeatability.

The HPPC current profile consists on 10-s duration, high constant current inputs with a 40-s open circuit in between. After the pulse sequence, the cell is immediately discharge with 10% DOD increments to traverse the SOC range and rested for 1hr before the pulse sequence is repeated [1]. This test sequence is repeated 9 times. Using a BSF of 94, the discharge and regen pulses correspond to a current of 5C (75 A) and 3.75C (56.25 A) respectively, and a 2C (30 A) discharge current to traverse the SOC range.

During the life cycle aging campaign, cells were stopped periodically for assessment using the procedures previously described (approximately every two weeks). All the characterization tests were conducted at 30 °C. Fig. 3 shows the voltage response during the capacity characterization tests for experiment # 16 in Table 1. The cell charge throughput expressed in kAh before each test is indicated in parenthesis.

[2] A C-rate is a measure of the rate at which a battery is charge/discharged relative to its maximum capacity. Operationally, C-rate = $I(t)/S_0$, where $I(t)$ is battery input current and S_0 is the battery nominal capacity.

[3] Aging campaign design by Ref. [13] and aged cells produced by the CAR Industrial Consortium/CARTech LLC.

[4] The Battery Size Factor (BSF) is defined as the minimum number of units (cells, modules or sub-batteries) of a given design required for a device to meet all U.S. Department of Energy Vehicle Technologies Program targets, including cycle life and calendar life [1].

[5] The HPPC test is conducted using a BSF of 94.

Table 1
Summary of aging experiments.

Experiment #	Operating mode	*Ratio* (t_{CD}:t_{CD+CS})	SOC_{min} [%]	Charging C-rate	Temperature [°C]	Charge throughput[a] [Ah]
1	Charge depleting	1	45	C/3	30	12,364
2		1	35	C/3	30	13,985
3		1	25	C/3	30	12,713
4		1	45	3C/2	30	24,361
5		1	35	3C/2	30	25,353
6		1	25	3C/2	30	27,597
7		1	45	5C	30	24,292
8		1	35	5C	30	28,141
9		1	25	5C	30	30,704
10	Charge sustaining	0	45	–	30	17,477
11		0	35	–	30	20,080
12		0	25	–	30	16,385
13	Mixed	1/2	35	3C/2	10	19,945
14		1/2	35	3C/2	30	20,719
15		1/4	35	3C/2	30	23,087
16		1/2	35	3C/2	45	21,316

[a] Attained by cell at the end of the experiment.

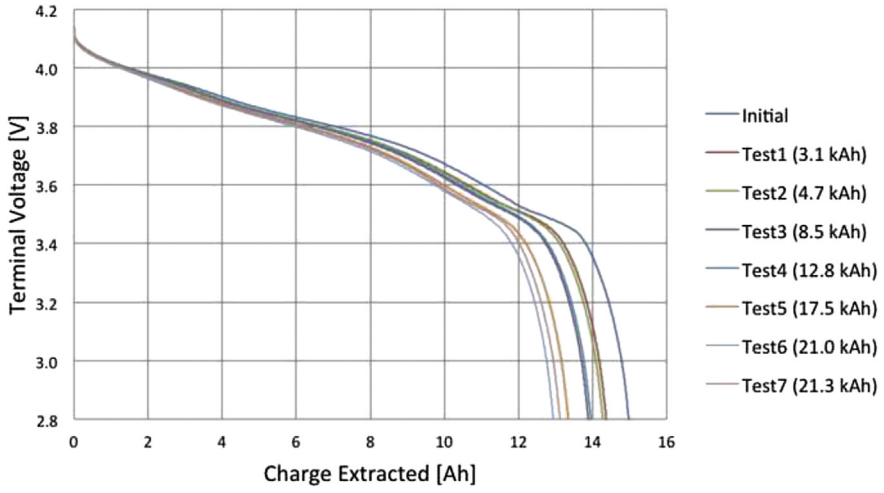

Fig. 3. Voltage response during the capacity characterization tests for experiment 16.

3. Capacity fade model development

In a battery, the number of cycles is commonly expressed using the total ampere-hour throughput [Ah] in both charge and discharge, i.e. $\mathrm{Ah} = \int_0^t |I(\tau)|\mathrm{d}\tau$, where $I(t)$ is the input current to the battery [42]. The capacity fade [%] of as a function of the battery charge throughput is then expressed as:

$$S_{\mathrm{loss}}(\mathrm{Ah}) = 100 \cdot \frac{S_0 - S(\mathrm{Ah})}{S_0} \tag{2}$$

where, S_0 is the cell nominal capacity and $S(\mathrm{Ah})$ is the cell capacity after $\mathrm{Ah} > 0$ charge throughput. It has been experimentally shown that the capacity fade in Li-ion batteries can be described using a power law relation with Ah [2,14,42]. Therefore, we adopt the following functional form for the capacity fade model,

$$S_{\mathrm{loss}}(\mathrm{Ah}) = f_C(\mathrm{SOC}_{\mathrm{min}}, \mathit{Ratio}, \mathrm{CR}, T) \cdot \mathrm{Ah}^z \tag{3}$$

where $f_C(\cdot)$ is a nonlinear function of the aging factors investigated during the aging campaign, and $z > 0$. Capacity characterization data are used to quantify the capacity fade for the model development. The capacity characterization points obtained from experiment i are fitted using the following expression:

$$S_{\mathrm{loss},i}(\mathrm{Ah}) = f_{C,i} \cdot \mathrm{Ah}^{z_i} \tag{4}$$

where, the coefficients $f_{C,i}$ and z_i are the fitting parameters for experiment i. The optimal fitting coefficients are found using the Nonlinear Optimization Toolbox in Matlab. In particular, the nonlinear Levenberg–Marquardt algorithm is used to solve the data fitting problem in the least-squares sense. For the model development, a constant $z = 0.48$, which corresponds to the average of the z_i is used [14,42]. The values of $f_{C,i}$ depend on the aging factors: *Ratio*, $\mathrm{SOC}_{\mathrm{min}}$, CR and T.

In the following subsections, the effect of each aging factor on capacity fade is studied and described. A semi-empirical model based on empirical relations of the relevant aging factors with capacity loss is developed and validated. The model is developed by fitting the experimental capacity severity factor data points $f_{C,i}$ into empirical relationships. All the data fitting problems are solved in the least-square sense and using Levenberg–Marquardt algorithm. The data obtained from experiment # 1 in Table 1 is discarded because it does not show consistency. This experiment is currently being repeated.

3.1. Dependence of capacity fade on charging rate

Lithium loss has been reported as one of the main mechanisms of capacity fade in Li-ion batteries during charging [37,43]. It is estimated that more than 90% of the cyclable lithium loss during a CC-CV charging occurs during the CV portion, while the rest occurs during the CC portion [43]. During CV, higher values end-of-charge voltage (EOCV) lead to higher rates of capacity fade [43]. It has been also reported that metallic plating and subsequent lithium loss can also occur during the CC portion even during a normal CC-CV charging if the charging current rate exceeds a certain value [37]. The experimental data obtained suggested that there is no significant dependence of capacity fade on CR under the charging conditions used during the experiments. This may be explained because the CRs used are relatively low (C/3, 2C/3 and 5C). Similarly, besides the use of the same CV (4.15 V) the EOCV reached while using CRs of C/3 and 2C/3 were pretty close, 4.117 V and 4.116 V respectively. Moreover, while using the CR of 5C ("fast charging"), the EOCV reached was 4.087 V, a lower voltage than with the other two CRs, which may have compensated, if any, the effect of using a higher CR. Therefore, the CR is not consider an stress factor for the development of the capacity fade model.

3.2. Dependence of capacity fade on temperature

After eliminating the CR from the stress factors, capacity fade may be affected by SOC_{min}, *Ratio* and *T*. It has been reported by different authors that the dependence of capacity fade on temperature is a combination of different aging effects [2,3,32]. On one hand, at high temperatures, capacity fade follows an Arrhenius relation with operating temperature, a relation which describes the effect of temperature on the chemical side reactions responsible for battery aging such as SEI film accumulation [1,3,26,28,35]. For different cathode materials the Arrhenius relation describes the dependence of capacity fade on aging for temperatures greater that 15 °C. On the other hand, at low temperatures, capacity fade may follow an exponential decay with operating temperature, probably related to metallic lithium plating and subsequent electrolyte decomposition by metallic Li [3,32]. Up to now, and to the best of our knowledge, this latter empirical relationship has not been fully understood and validated with experimental data. For this reason and since the experimental campaign conducted in this work was not intended to fully understand this latter phenomenon, the experimental point corresponding to 10 °C is not used for the aging model development. Therefore, the following expression for capacity loss is adopted:

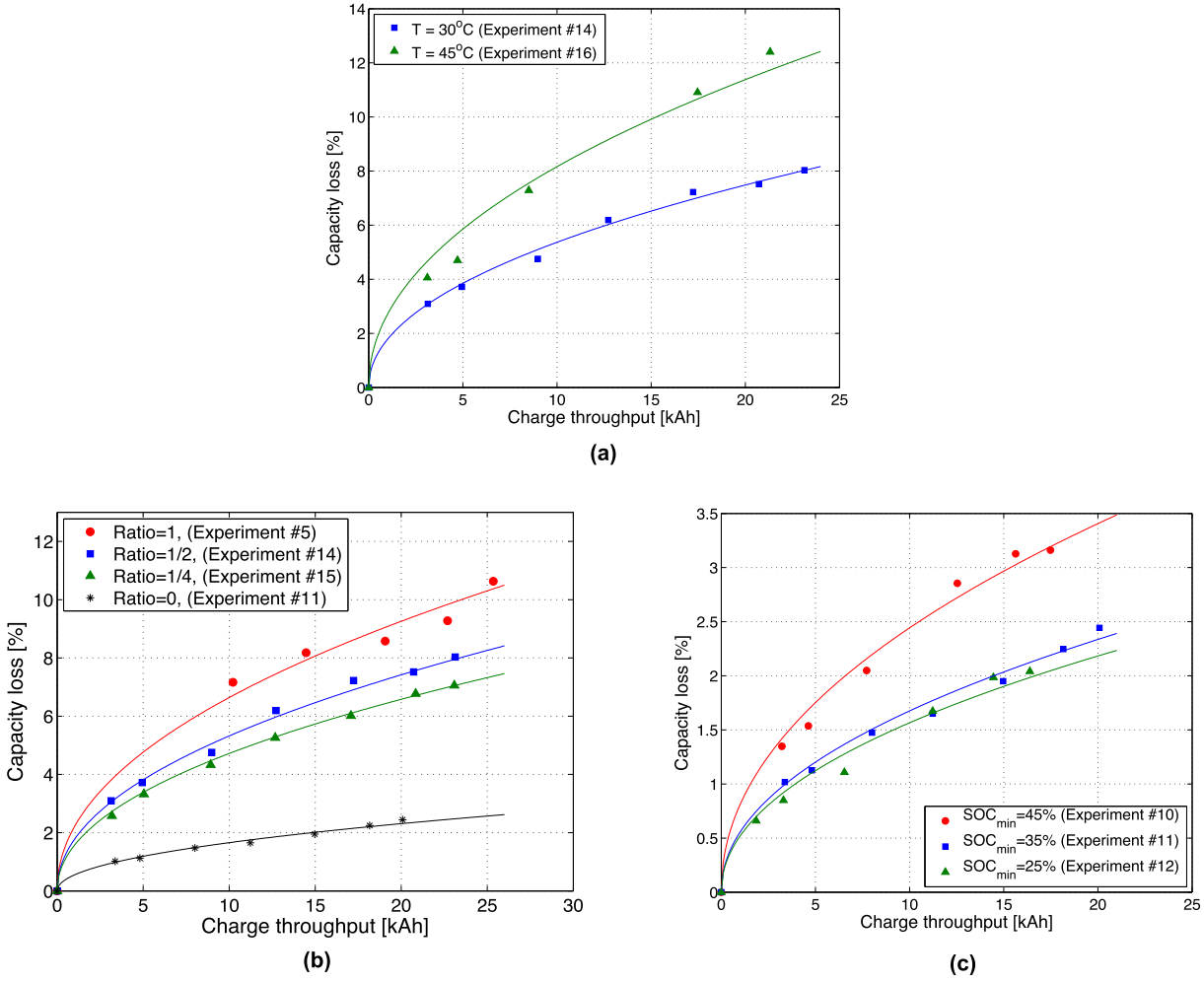

Fig. 4. Capacity loss for: (a) temperature experiments; (b) *Ratio* experiments; (c) SOC_{min} experiments (all conducted with a *Ratio* of 0). Experimental data are shown as markers, and the model, as solid curve.

$$S_{loss}(\text{Ah}) = f_C(\text{SOC}_{min}, Ratio, T)\cdot \text{Ah}^z \quad (5)$$

where, $f_C(\cdot)$ is the capacity severity factor function defined as [2,26]:

$$f_C(\cdot) = a_C(\text{SOC}_{min}, Ratio)\cdot \exp\left(\frac{-E_{a_C}}{R_g T}\right) \quad (6)$$

where, E_{a_C} is the cell activation energy for the capacity fade process, R_g is the is the universal gas constant, and T is the cell absolute temperature.

The data from the temperature experiments along with the best curve fittings are shown in Fig. 4(a). The experiments correspond to a *Ratio* of 1/2, SOC_{min} = 35% and a charging rate of 3C/2, at two different temperatures, $T_1 = 30\,^{\circ}\text{C}$ and $T_2 = 45\,^{\circ}\text{C}$ (Experiments # 14 and # 16 respectively, see Table 1). The data from these experiments along with Equation (6) is used to find the value of E_{a_C}. The following relationship is used:

$$\ln\left[\frac{f_C(35\%, 0.5, T_1)}{f_C(35\%, 0.5, T_2)}\right] = \frac{-E_{a_C}}{R_g}\cdot\left(\frac{1}{T_1} - \frac{1}{T_2}\right) \quad (7)$$

where, the values of f_C(35%,0.5,T_1) and f_C(35%,0.5,T_2) correspond to the optimal coefficients obtained from the data curve fitting and ln is the natural logarithm function. The activation energy obtained for the capacity fade process is $E_{a_C} = 22406$ [J mol^{-1}]. The rate of capacity fade increases while increasing the operating temperature for the temperature range under study.

3.3. Dependence of capacity fade on ratio

The experiments conducted to study the influence of the *Ratio* on capacity loss correspond to experiments # 5, 11, 14 and 15 in Table 1. The experiments were conducted at SOC_{min} = 35%, $T = 30\,^{\circ}\text{C}$, and ratios of 0, 1/4, 1/2 and 1, respectively. The experimental severity factor values are fitted to the following equation:

$$a_C(35\%, Ratio) = \alpha_1 + \beta\cdot(Ratio)^b \quad (8)$$

where, $\alpha_1 = 145$, $\beta = 420$ and $b = 0.34$ are the identified constants. Fig. 5 shows the severity factor obtained form the experimental data best curve fittings, and the proposed empirical relationship for the dependence of capacity fade on the *Ratio*. The results of these experiments indicate that the rate of capacity fade increases while increasing the *Ratio*. The rate of capacity fade is the lowest at CS operating mode i.e. *Ratio* of 0 and increases rapidly while increasing the ratio, reaching the highest value during CD operation i.e. *Ratio* of 1. Fig. 4(b) shows the capacity characterization points obtained from experiments # 5, 11, 14 and 15 as markers, and the proposed empirical relationship, as solid curve. The results experiments # 2, 5 and 8, are used to validate the proposed model. Fig. 6 shows the experimental data obtained from these experiments and the proposed empirical relationship. The experimental data points show good fitting with the proposed empirical relationship.

3.4. Dependence of capacity fade on SOC_{min}

The experiments conducted to study the influence of SOC_{min} on capacity fade correspond to experiments # 10, 11, and 12 in Table 1. The experiments were conducted at $T = 30\,^{\circ}\text{C}$, with a *Ratio* of 0, and SOC_{min} of 45, 35 and 25%, respectively. The experimental capacity severity factor values are fitted to the following equation,

$$a_C(\text{SOC}_{min}, 0) = \alpha_2 + \gamma\cdot(\text{SOC}_{min} - \text{SOC}_0)^c \quad (9)$$

where $\alpha_2 = 137$ and $\gamma = 9610$ are the identified constants for $\text{SOC}_0 = 0.25$ and $c = 3$. Fig. 7 shows the capacity severity factor points obtained from the experimental data best curve fittings, and the proposed empirical relationship for the dependence of capacity fade on SOC_{min}. The results of these experiments indicate that the rate of capacity fade increases while increasing SOC_{min}, this effect is more pronounced for $\text{SOC}_{min} > 35\%$. Fig. 4(c) shows the capacity characterization points obtained from these experiments and the proposed empirical relationship.

4. Capacity fade model

Summarizing, capacity fade can be described by:

$$S_{loss}(\text{Ah}) = a_C(\text{SOC}_{min}, Ratio)\cdot \exp\left(\frac{-E_{a_C}}{R_g T}\right)\cdot \text{Ah}^z \quad (10)$$

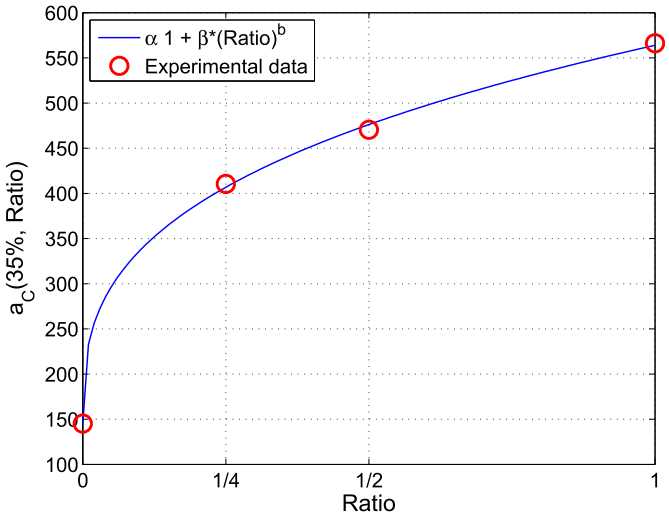

Fig. 5. Capacity severity factor function from *Ratio* experiments. Capacity severity factor points obtained form the experimental data best curve fittings are shown as markers, and the model, as solid curve (Equation (8)).

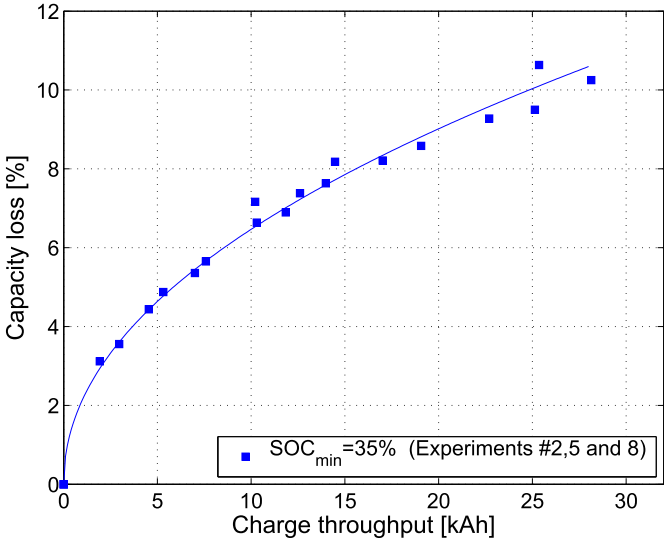

Fig. 6. Capacity loss for all the experiments conducted with a *Ratio* of 1 at SOC_{min} = 35%. Experimental data are shown as markers, and the model, as solid curve.

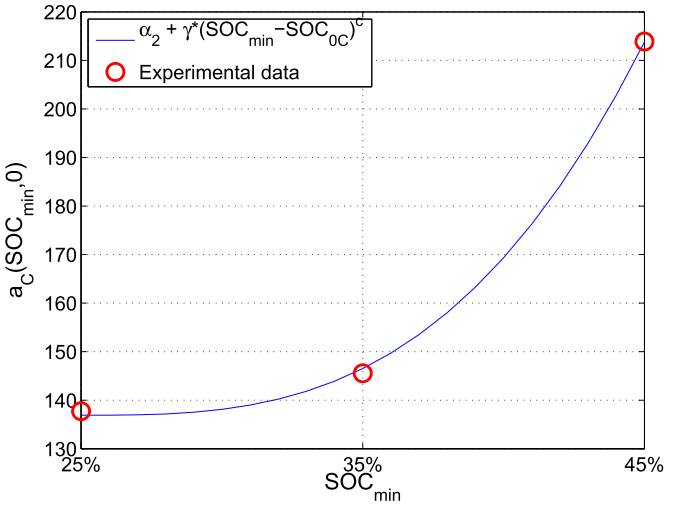

Fig. 7. Capacity severity factor function from SOC_{min} experiments, all conducted with a *Ratio* of 0. Capacity severity factor points obtained form the experimental data best curve fittings are shown as markers, and the model, as solid curve (Equation (9)).

where, $a_C(\cdot)$ is the capacity severity factor function given by:

$$a_C(\cdot) = \alpha_C + \beta_C \cdot (Ratio)^b + \gamma_C \cdot (SOC_{min} - SOC_0)^c \tag{11}$$

where, the dimensionless constant coefficients α_C,β_C,γ_C,b,c,z, SOC_{0C}, and the dimensional constant coefficients R_u and E_{a_C} and are given by:

$$\left\{\begin{array}{c} \alpha_C = 137 \\ \beta_C = 420 \\ \gamma_C = 9610 \\ b = 0.34 \\ c = 3 \\ z = 0.48 \\ SOC_0 = 0.25 \\ E_{a_C} = 22406 \quad [\mathrm{Jmol^{-1}}] \\ R_g = 8.314 \quad [\mathrm{JK^{-1}mol^{-1}}] \end{array}\right\} \tag{12}$$

Fig. 8 shows the fitted surface $a_C(\cdot)$ that describes the dependence of capacity fade on SOC_{min} and *Ratio*. The capacity characterization data points from experiments # 1,4,3,6 and 9 in Table 1 are used to validate the model. All conducted at $T = 30\ ^{\circ}C$ with a *Ratio* of 1. Experiments # 3,6 and 9 with $SOC_{min} = 25\%$, while experiments # 1 and 4 with $SOC_{min} = 45\%$. Fig. 9 shows the experimental points obtained from these experiments and the proposed model. The proposed empirical capacity fade model shows consistency with the experimental data points used for validation.

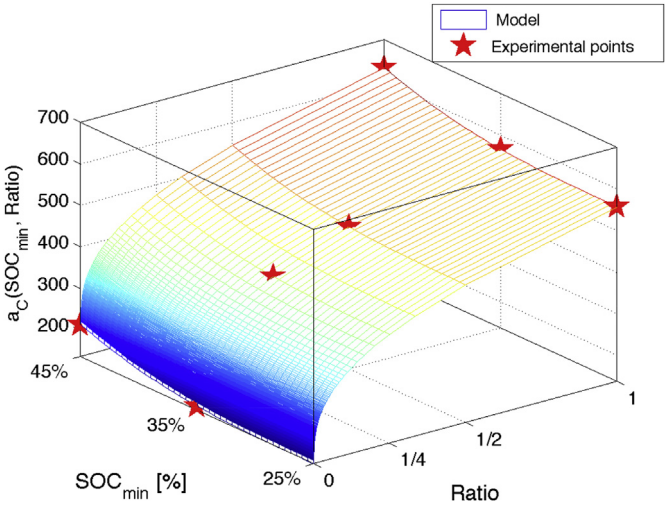

Fig. 8. Capacity severity factor map. The experimental points are shown as markers, and the severity function, as solid surface (Equation (11)).

The goodness of fit for the capacity fade model is evaluated through the root mean square (RMS) error defined as:

$$RMS_S = \sqrt{\frac{\sum_{\substack{1<i<N \\ 1<j<m_i}} \left(\widehat{S}_{loss,i}(Ah_j) - S_{loss,i}(Ah_j)\right)^2}{\sum_{\substack{1<i<N \\ 1<j<m_i}} 1}} \tag{13}$$

where, $\widehat{S}_{loss,i}(Ah_j)$ is the estimated capacity loss for experiment #i at Ah_j charge throughput, $S_{loss,i}(Ah_j)$ is the corresponding experimental point, N is the total number of experiments, and m_i is the total number of capacity assessment tests conducted during experiment #i (including initial, final and periodical state of health characterization tests). The root mean square obtained is $RMS_S = 0.0047\%$.

The capacity fade process follows a power law with the ampere-hour throughput. The power law factor, z, is very close to 0.5, which indicates that one of the main mechanisms of capacity fade may be the growth of a solid electrolyte (SEI) layer, causing a square root of Ah shaped behavior [26,35]. Usually SEI growth takes place mainly at the beginning of cycling and continues steadily with cycling [3]. Capacity fade follows Arrhenius-like kinetics, which indicates that it may be caused by thermally activated process.

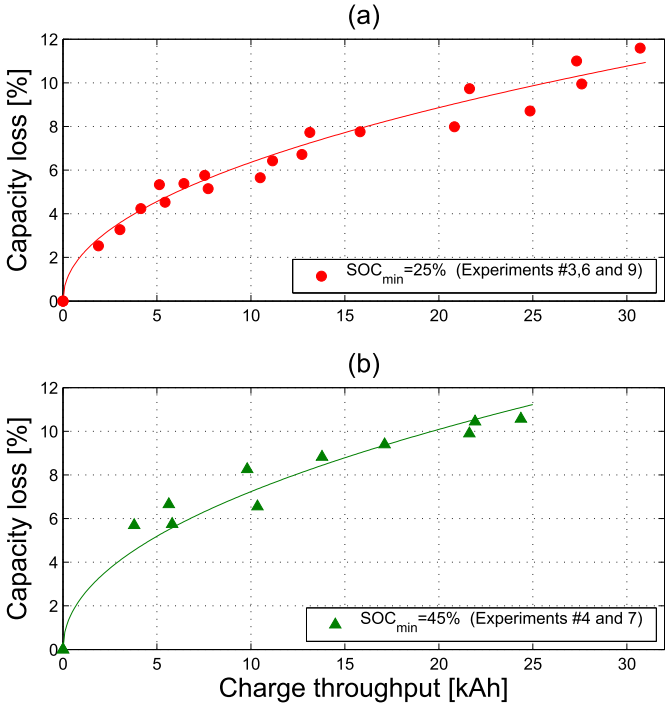

Fig. 9. Capacity loss for SOC_{min} experiments, all conducted with a *Ratio* of 1. Experimental data are shown as markers, and the model, as solid curve (Equation (11)), (a) Experiments conducted with $SOC_{min} = 25\%$, (b) Experiments conducted with $SOC_{min} = 45\%$.

5. Power fade model development

The internal resistance increase of a battery cell [%] as a function of ampere-hour throughput can be expressed as:

$$R_{\text{inc}}(\text{Ah}) = 100 \cdot \frac{R(\text{Ah}) - R_0}{R_0} \tag{14}$$

where, R_0 is the cell nominal internal resistance and $R(\text{Ah})$ is the cell internal resistance after Ah > 0 charge throughput. From observations of the obtained experimental data and aging studies reported in the literature the resistance increase in Li-ion batteries can be described using a linear relation with Ah [39]. Therefore, we adopt the following functional form for the resistance increase model:

$$R_{\text{inc}}(\text{Ah}) = f_R(\text{SOC}_{\text{min}}, Ratio, \text{CR}, T) \cdot \text{Ah} \tag{15}$$

where $f_R(\cdot)$ is a nonlinear function of the aging factors.

In a battery cell, the internal resistance is a function of the operational conditions: SOC, temperature and input current, charge/discharge [44]. There are different methods to calculate the internal resistance of a battery cell. For example, HPPC test, identification techniques using an equivalent circuit models of the battery cell, or using the input–output cell response and Ohm's law [1,44]. The first two methods are not suitable for online applications, for this reason the third approach is selected to analyze the data. Using the experimental data, the battery cell internal resistance is calculated by observing the voltage response to every input current step increase/decrease and using Ohm's law as follows [45]:

$$\widehat{R} = \frac{\Delta V}{\Delta I} = \left| \frac{V_{\text{final}} - V_{\text{initial}}}{I_{\text{final}} - I_{\text{initial}}} \right| \tag{16}$$

As illustration, a schematic of the input current and cell voltage response during the first 100 s of a CD micro-duty cycle are shown in Fig. 10. In the figure, the initial currents and voltages used for the resistance calculations are shown as square markers; the final currents and voltages as triangle markers; and the input current and voltage response as solid curves.

In order to reduce noise and capture the actual trend in resistance increase, outlier removal and filtering methods were applied.

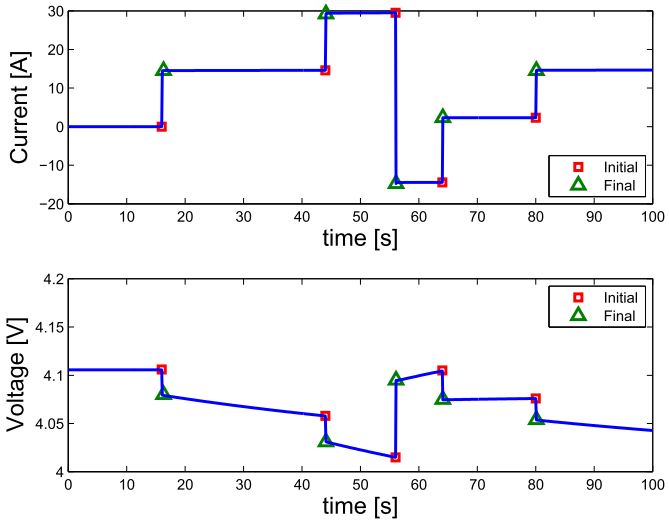

Fig. 10. Schematic of the input current and cell voltage response during the first 100 s of a CD micro-duty cycle. The initial currents and voltages used for the resistance calculations are shown as square markers; the final currents and voltages as triangle markers; and the input current and voltage response as solid curves.

Resistance values greater than 3 standard deviations from the average were removed to reduce resemblance. The cutoff criteria was chosen to remove false resistance values and not to remove data that did not fit the normal distribution. The removed values, which were not representative of the overall trend, typically constituted less than 1% of the total set. After the outlier removal, a moving average technique was chosen to capture the actual trend in resistance growth. The moving average window used has a length of 250 points.

Fig. 11 shows the resistance data from experiment # 16 before and after the outlier removal and filtering. Similar resistance data processing results are obtained for the rest of the experiments. These simple calculations do not perfectly identify the actual value of the internal resistance; however, they provide a simple but still accurate approach to trace the overall trend of the resistance growth throughout the battery lifespan.

Resistance data processed as explained above are used to quantify the growth in internal resistance for the model development. The resistance points obtained from experiment i are fitted using the following expression:

$$R_{\text{inc},i}(\text{Ah}) = f_{R,i} \cdot \text{Ah} \tag{17}$$

where, the coefficients $f_{R,i}$ is the fitting parameter. The fitting coefficients are found using a linear least squares approach. In the following subsections, the influence of the stress factors on the resistance growth is studied. Since the approach for the model development is similar to the one used for the capacity fade model, just the main highlights are presented in the next subsections.

5.1. Dependence of resistance increase on charging rate

In contrast to the capacity fade process, the experimental data suggest that there is dependence of resistance increase on the CR. For this reason, CR is considered a stress factor for the model development in this case.

5.2. Dependence of resistance increase on temperature

Following a similar approach as in Subsection 3.2 the following expression is used to describe the dependence of resistance increase on temperature:

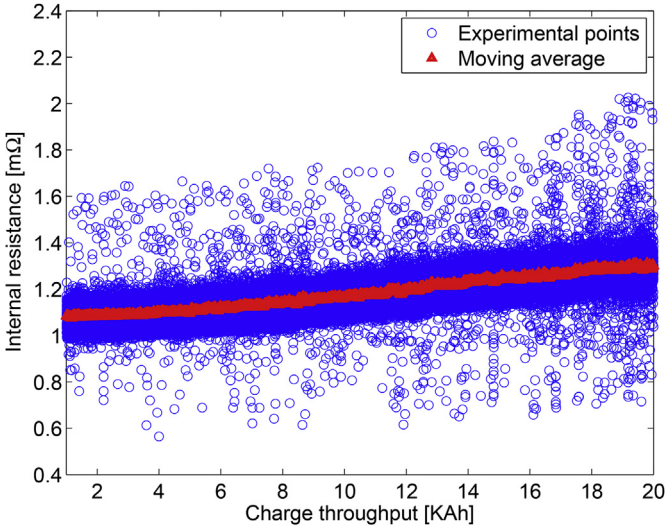

Fig. 11. Resistance data from experiment #16 before and after the outlier removal and filtering.

$$R_{\text{inc}}(\text{Ah}) = a_R(\text{SOC}_{\min}, Ratio, \text{CR}) \cdot \exp\left(\frac{-E_{a_R}}{R_u T}\right) \cdot \text{Ah} \quad (18)$$

where, $a_R(\cdot)$ is the resistance severity factor function which depend on $\text{SOC}_{\min}$, *Ratio*, CR; E_{a_R} is the cell activation energy for the resistance increase process; R_u is the is the universal gas constant; and T is the cell absolute temperature. The activation energy obtained for the resistance growth process is $E_{a_R} = 51800 \quad [\text{J mol}^{-1}]$. Fig. 12(a) shows the resistance characterization points obtained from experiments as markers, and the model, as solid curve. The rate of resistance growth increases while increasing the operating temperature for the temperature range under study.

5.3. Dependence of resistance increase on ratio

The experiments conducted to study the influence of *Ratio* on resistance increase correspond to experiments # 5, 11, 14 and 15 in Table 1. These experiments were conducted at *Ratios* of 0, 1/4, 1/2 and 1, respectively. The experimental severity factor values obtained for *Ratios* of 1/4, 1/2 and 1 may be consider the same while the one obtained for *Ratio* = 0 is significantly different from the others. This result suggest that the underlying influence of *Ratio* on resistance increase is the fact that during CS the battery is not fully charged (during CS the battery is operated during a narrow SOC window). Therefore, for the model development a "equivalent" CR of zero is assigned for the CS operation. Therefore, the following equivalent CR function is defined:

$$\text{CR}_{\text{eq}}(Ratio) = \begin{cases} 0 & Ratio = 0 \\ \text{CR} & Ratio > 0 \end{cases} \quad (19)$$

6. Resistance increase model

Summarizing the results from the model development, the resistance growth can be described by:

$$R_{\text{inc}}(\text{Ah}) = a_R(\text{SOC}_{\min}, Ratio, \text{CR}) \cdot \exp\left(\frac{-E_{aR}}{R_u T}\right) \cdot \text{Ah} \quad (20)$$

where, $a_R(\cdot)$ is the resistance severity factor function given by:

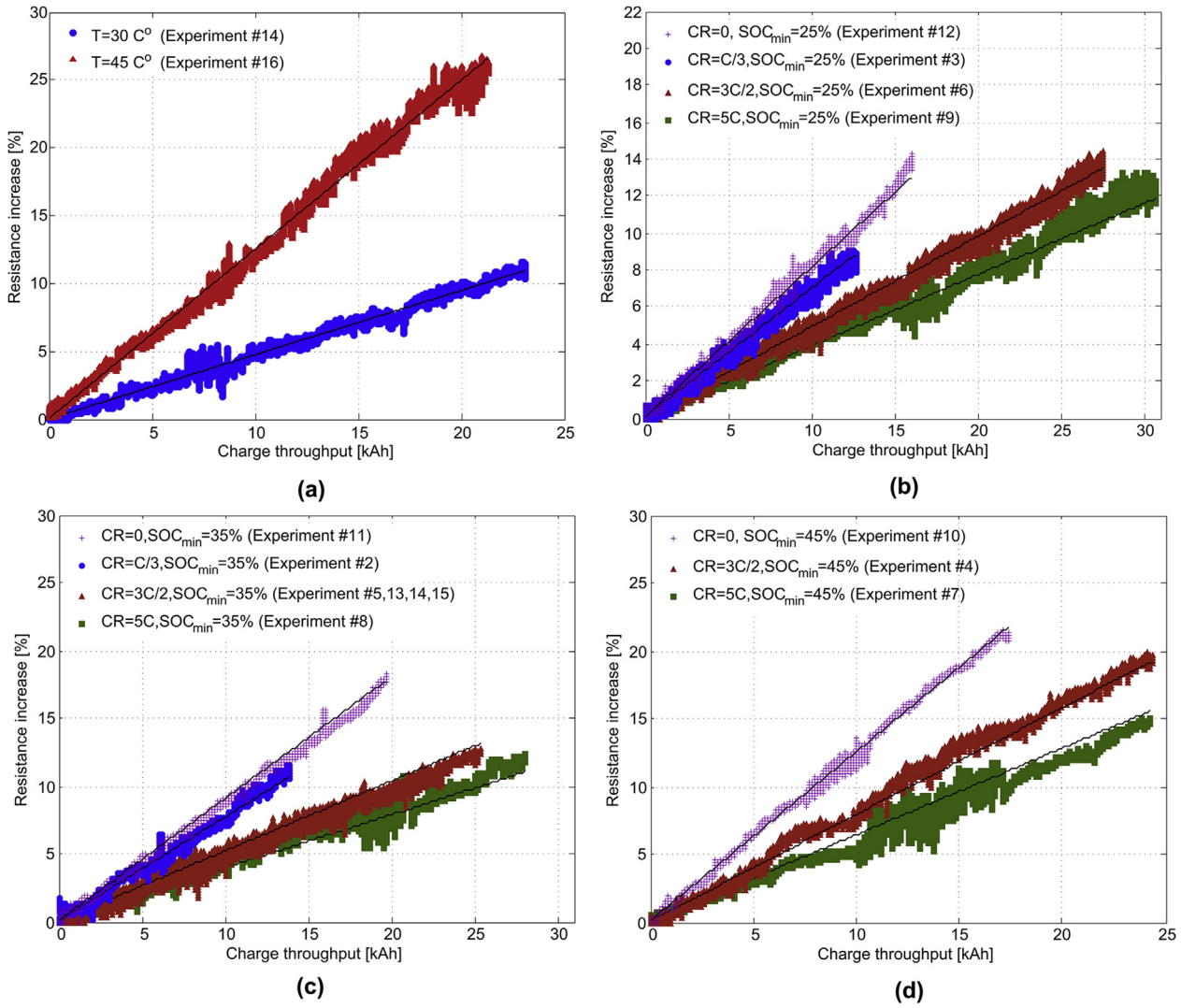

Fig. 12. Resistance increase for: (a) temperature experiments; (b) $\text{SOC}_{\min} = 25\%$ experiments, $T = 30\ ^\circ\text{C}$; (c) $\text{SOC}_{\min} = 35\%$ experiments, $T = 30\ ^\circ\text{C}$; (d) $\text{SOC}_{\min} = 45\%$ experiments, $T = 30\ ^\circ\text{C}$. Experimental data are shown as markers, and the model, as solid curve.

$$a_R(\cdot) = \alpha_R + \beta_R \cdot (\mathrm{SOC_{min}} - \mathrm{SOC_0})^{c_R} + \gamma_R \cdot \exp\left[d \cdot (\mathrm{CR_0} - \mathrm{CR_{eq}}) + e \cdot (\mathrm{SOC_{min}} - \mathrm{SOC_0})\right] \tag{21}$$

where, $\mathrm{CR_{eq}}$ is a function of *Ratio* given by:

$$\mathrm{CR_{eq}}(Ratio) = \begin{cases} 0 & Ratio = 0 \\ \mathrm{CR} & Ratio > 0 \end{cases} \tag{22}$$

and, the dimensionless constant coefficients α_R,β_R,γ_R,c_R,d,e, $\mathrm{SOC_0}$ and the dimensional constant coefficients R_u and E_{a_R} and are given by:

$$\left\{ \begin{array}{c} \alpha_R = 3.2053e+05 \\ \beta_R = 1.3674e+09 \\ \gamma_R = 3.6342e+03 \\ c_R = 5.45 \\ d = 0.9179 \\ e = 1.8277 \\ \mathrm{SOC_0} = 0.25 \\ \mathrm{CR_0} = 5 \\ E_{aR} = 51800 \quad \left[\mathrm{J\,mol^{-1}}\right] \\ R_g = 8.314 \quad \left[\mathrm{J\,K^{-1}mol^{-1}}\right] \end{array} \right\} \tag{23}$$

Fig. 13 shows the resistance severity factor surface $a_R(\cdot)$ that describes the dependence of resistance growth on $\mathrm{SOC_{min}}$ and $\mathrm{CR_{eq}}$. The results indicate that the rate in resistance growth increases while increasing $\mathrm{SOC_{min}}$, and the rate in resistance growth increases while decreasing $\mathrm{CR_{eq}}$. Fig. 12(b,c,d) show the resistance characterization points obtained from experiments # 2 to 12 and # 14,16 along with the proposed model.

Since the model objective in this case is to capture the trend on the resistance growth and not to predict the instantaneous value of the battery internal resistance; the goodness of fit for the model is evaluated through (RMS) error defined over the resistance severity factor as:

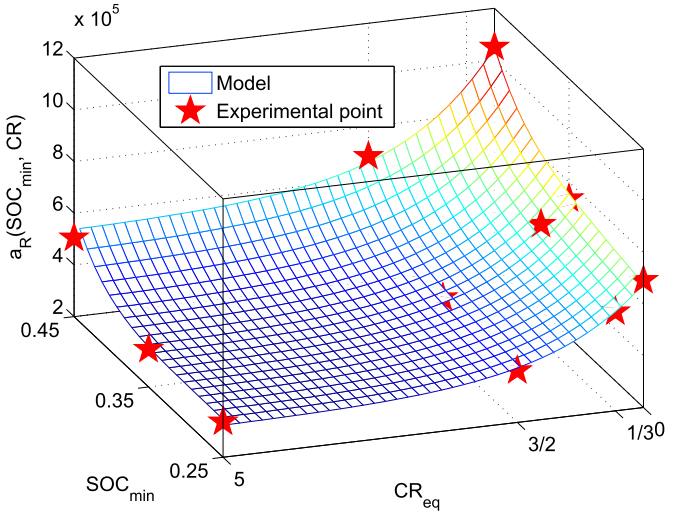

Fig. 13. Resistance severity factor surface. Resistance severity factor points obtained form the experimental data best curve fittings are shown as markers, and the model, as solid surface (Equation (21)).

$$\mathrm{RMS_R} = \sqrt{\frac{\sum_{1<i<N}\left(\widehat{f}_{R,i} - f_{R,i}\right)^2}{N}} \tag{24}$$

where, $\widehat{f}_{R,i}$ is the estimated severity factor for experiment #*i*, $f_{R,i}$ is their corresponding experimental severity factor point, and N is the total number of experiments. The root mean square obtained is $\mathrm{RMS_R} = 2.0495e{-}05$.

The resistance increase process follows a linear relationship with Ah. Additionally, the power loss process follows an Arrhenius-like kinetics, which indicates that the resistance growth may be caused by a thermally activated process.

7. Conclusions

This paper presented the results of a experimental campaign conducted on Li-ion pouch cells with NMC-LMO positive electrodes. During the campaign the influence of charge sustaining/depleting operation, minimum SOC, charging rate and temperature on the aging process is studied. The results show that capacity fade and resistance increase are influenced by *Ratio*, $\mathrm{SOC_{min}}$, CR and temperature. Using a non-linear curve fitting technique, a semi-empirical aging model which describes the capacity fade and resistance increase as a function of the influencing stress factors and the ampere-hour throughput was proposed based on the experimental data. The proposed aging model is indented to be used for predicting battery cycle-life under realistic PHEV operation. For its simplicity but still good accuracy, the model can be used for the design and sizing of PHEV energy storage systems; for the design and implementation of algorithms for battery state-of-health assessment and end-of-life prediction (prognosis); as part of PHEV optimal energy management schemes including battery aging, among others. The aging model may be also used for more research-oriented purposes such as the study the propagation of aging among cells in battery systems.

Disclaimer

Acknowledgments

The authors wish to thank the CAR Industrial Consortium[6]/ CARTech LLC for producing the aged cells. This material is based upon work supported by the National Science Foundation under Grant Number NSF-1301238 and the Department of Energy under Award Number DE-PI0000012.

References

[1] Anonymous, United States Department of Energy Battery Test Manual for Plug-in Hybrid Electric Vehicles, Inl/ext-07-12536, Rev 2 Edition, December 2010.
[2] J. Wang, P. Liu, J. Hicks-Garner, E. Sherman, S. Soukiazian, M. Verbrugge, H. Tataria, J. Musser, P. Finamore, Cycle-life model for graphite-lifepo4 cells, J. Power Sources 196 (8) (2011) 3942–3948.
[3] J. Vetter, P. Novák, M. Wagner, C. Veit, K.-C. Möller, J. Besenhard, M. Winter, M. Wohlfahrt-Mehrens, C. Vogler, A. Hammouche, Ageing mechanisms in lithium-ion batteries, J. Power Sources 147 (1–2) (2005) 269–281.
[4] S. Onori, P. Spagnol, V. Marano, Y. Guezennec, G. Rizzoni, A new life estimation method for lithium-ion batteries in plug-in hybrid electric vehicles applications, Int. J. Power Electron. 4 (4) (2012) 302–319.
[5] M. Wohlfahrt-Mehrens, C. Vogler, J. Garche, Aging mechanisms of lithium cathode materials, J. Power Sources 127 (1–2) (2004) 58–64.
[6] C.Y. Wang, W.B. Gu, B.Y. Liaw, Micro macroscopic coupled modeling of batteries and fuel cells: I. model development, J. Electrochem. Soc. 145 (10) (1998) 3407–3417.
[7] R. Spotnitz, Simulation of capacity fade in lithium-ion batteries, J. Power Sources 113 (1) (2003) 72–80.
[8] P. Ramadass, B. Haran, R. White, B.N. Popov, Mathematical modeling of the capacity fade of Li-ion cells, J. Power Sources 123 (2) (2003) 230–240.
[9] S. Santhanagopalan, Q. Guo, P. Ramadass, R.E. White, Review of models for predicting the cycling performance of lithium ion batteries, J. Power Sources 156 (2) (2006) 620–628.
[10] T. Yoshida, M. Takahashi, S. Morikawa, C. Ihara, H. Katsukawa, T. Shiratsuchi, J.-i. Yamaki, Degradation mechanism and life prediction of lithium-ion batteries, J. Electrochem. Soc. 153 (3) (2006) A576–A582.
[11] M. Safari, M. Morcrette, A. Teyssot, C. Delacourt, Life-prediction methods for lithium-ion batteries derived from a fatigue approach: I. introduction: capacity-loss prediction based on damage accumulation, J. Electrochem. Soc. 157 (6) (2010) A713–A720.
[12] M. Safari, M. Morcrette, A. Teyssot, C. Delacourt, Life prediction methods for lithium-ion batteries derived from a fatigue approach: Li. capacity-loss prediction of batteries subjected to complex current profiles, J. Electrochem. Soc. 157 (7) (2010) A892–A898.
[13] J. Marcicki, A. Bartlett, M. Canova, A.T. Conlisk, G. Rizzoni, Y. Guezennec, X.G. Yang, T. Miller, Characterization of cycle-life aging in automotive lithium-ion pouch cells, in: Meeting Abstracts, No. 10, the Electrochemical Society, 2012, pp. 1090–1098.
[14] F. Todeschini, S. Onori, G. Rizzoni, An experimentally validated capacity degradation model for li-ion batteries in phevs application, in: 8th IFAC Symposium on Fault Detection, Supervision and Safety of Technical Processes, IFAC, 2012.
[15] K. Goebel, B. Saha, A. Saxena, J. Celaya, J. Christophersen, Prognostics in battery health management, Instrum. Meas. Mag. IEEE 11 (4) (2008) 33–40.
[16] L. Serrao, S. Onori, A. Sciarretta, Y. Guezennec, G. Rizzoni, Optimal energy management of hybrid electric vehicles including battery aging, in: American Control Conference (ACC), 2011, 2011, pp. 2125–2130.
[17] S. Ebbesen, P. Elbert, L. Guzzella, Battery state-of-health perceptive energy management for hybrid electric vehicles, Veh. Technol. IEEE Trans. 61 (7) (2012) 2893–2900.
[18] A. Cordoba-Arenas, S. Onori, R. Giorgio, G. Fan, Aging propagation in advanced battery systems: preliminary results, in: IFAC Symposium Advances in Automotive Control, Japan, September, 2013.
[19] J.W. Fergus, Recent developments in cathode materials for lithium ion batteries, J. Power Sources 195 (4) (2010) 939–954.
[20] P. Albertus, J. Christensen, J. Newman, Experiments on and modeling of positive electrodes with multiple active materials for lithium-ion batteries, J. Electrochem. Soc. 156 (7) (2009) A606–A618.
[21] K.-W. Nam, W.-S. Yoon, H. Shin, K.Y. Chung, S. Choi, X.-Q. Yang, In situ x-ray diffraction studies of mixed $limn_2o_4$–$lini_{1/3}co_{1/3}mn_{1/3}o_2$ composite cathode in Li-ion cells during charge-discharge cycling, J. Power Sources 192 (2) (2009) 652–659.
[22] M. Dubarry, C. Truchot, M. Cugnet, B.Y. Liaw, K. Gering, S. Sazhin, D. Jamison, C. Michelbacher, Evaluation of commercial lithium-ion cells based on composite positive electrode for plug-in hybrid electric vehicle applications. part i: Initial characterizations, J. Power Sources 196 (23) (2011) 10328–10335.
[23] Z.F. Ma, X.Q. Yang, X.Z. Liao, X. Sun, J. McBreen, Electrochemical evaluation of composite cathodes base on blends of $limn_2o_4$ and $lini_{0.8}co_{0.2}o_2$, Electrochem. Commun. 3 (8) (2001) 425–428.
[24] M. Broussely, S. Herreyre, P. Biensan, P. Kasztejna, K. Nechev, R. Staniewicz, Aging mechanism in li ion cells and calendar life predictions, J. Power Sources 97-98 (0) (2001) 13–21.
[25] M. Broussely, P. Biensan, F. Bonhomme, P. Blanchard, S. Herreyre, K. Nechev, R. Staniewicz, Main aging mechanisms in li ion batteries, J. Power Sources 146 (1–2) (2005) 90–96.
[26] I. Bloom, B. Cole, J. Sohn, S. Jones, E. Polzin, V. Battaglia, G. Henriksen, C. Motloch, R. Richardson, T. Unkelhaeuser, D. Ingersoll, H. Case, An accelerated calendar and cycle life study of Li-ion cells, J. Power Sources 101 (2) (2001) 238–247.
[27] I. Bloom, S.A. Jones, E.G. Polzin, V.S. Battaglia, G.L. Henriksen, C.G. Motloch, R.B. Wright, R.G. Jungst, H.L. Case, D.H. Doughty, Mechanisms of impedance rise in high-power, lithium-ion cells, J. Power Sources 111 (1) (2002) 152–159.
[28] R. Wright, C. Motloch, J. Belt, J. Christophersen, C. Ho, R. Richardson, I. Bloom, S. Jones, V. Battaglia, G. Henriksen, T. Unkelhaeuser, D. Ingersoll, H. Case, S. Rogers, R. Sutula, Calendar- and cycle-life studies of advanced technology development program generation 1 lithium-ion batteries, J. Power Sources 110 (2) (2002) 445–470.
[29] R.P. Ramasamy, R.E. White, B.N. Popov, Calendar life performance of pouch lithium-ion cells, J. Power Sources 141 (2) (2005) 298–306.
[30] B.Y. Liaw, R.G. Jungst, G. Nagasubramanian, H.L. Case, D.H. Doughty, Modeling capacity fade in lithium-ion cells, J. Power Sources 140 (1) (2005) 157–161, http://dx.doi.org/10.1016/j.jpowsour.2004.08.017.
[31] M. Dubarry, V. Svoboda, R. Hwu, B.Y. Liaw, Capacity and power fading mechanism identification from a commercial cell evaluation, J. Power Sources 165 (2) (2007) 566–572.
[32] W. Prochazka, G. Pregartner, M. Cifrain, Design-of-experiment and statistical modeling of a large scale aging experiment for two popular lithium ion cell chemistries, J. Electrochem. Soc. 160 (8) (2013) A1039–A1051.
[33] I. Bloom, L.K. Walker, J.K. Basco, D.P. Abraham, J.P. Christophersen, C.D. Ho, Differential voltage analyses of high-power lithium-ion cells. 4. cells containing nmc, J. Power Sources 195 (3) (2010) 877–882.
[34] M. Ecker, J.B. Gerschler, J. Vogel, S. Käbitz, F. Hust, P. Dechent, D.U. Sauer, Development of a lifetime prediction model for lithium-ion batteries based on extended accelerated aging test data, J. Power Sources 215 (0) (2012) 248–257.
[35] S. Käbitz, J.B. Gerschler, M. Ecker, Y. Yurdagel, B. Emmermacher, D. André, T. Mitsch, D.U. Sauer, Cycle and calendar life study of a graphite $lini_{1/3}mn_{1/3}co_{1/3}o_2$ Li-ion high energy system. part a: full cell characterization, J. Power Sources 239 (0) (2013) 572–583.
[36] S.B. Peterson, J. Apt, J. Whitacre, Lithium-ion battery cell degradation resulting from realistic vehicle and vehicle-to-grid utilization, J. Power Sources 195 (8) (2010) 2385–2392.
[37] S.S. Zhang, The effect of the charging protocol on the cycle life of a Li-ion battery, J. Power Sources 161 (2) (2006) 1385–1391.
[38] M. Uno, K. Tanaka, Influence of high-frequency charge -discharge cycling induced by cell voltage equalizers on the life performance of lithium-ion cells, Veh. Technol. IEEE Trans. 60 (4) (2011) 1505–1515.
[39] J. Belt, V. Utgikar, I. Bloom, Calendar and *phev* cycle life aging of high-energy, lithium-ion cells containing blended spinel and layered-oxide cathodes, J. Power Sources 196 (23) (2011) 10213–10221.
[40] K.L. Gering, S.V. Sazhin, D.K. Jamison, C.J. Michelbacher, B.Y. Liaw, M. Dubarry, M. Cugnet, Investigation of path dependence in commercial lithium-ion cells chosen for plug-in hybrid vehicle duty cycle protocols, J. Power Sources 196 (7) (2011) 3395–3403.
[41] M. Dubarry, C. Truchot, B.Y. Liaw, K. Gering, S. Sazhin, D. Jamison, C. Michelbacher, Evaluation of commercial lithium-ion cells based on composite positive electrode for plug-in hybrid electric vehicle applications. part ii. degradation mechanism under 2 c cycle aging, J. Power Sources 196 (23) (2011) 10336–10343.
[42] L. Serrao, S. Onori, G. Rizzoni, Y. Guezennec, Model based strategy for estimation of the residual life of automotive batteries, in: 7th IFAC Symposium on Fault Detection, Supervision and Safety of Technical Processes, IFAC, 2009, pp. 923–928.
[43] G. Ning, R.E. White, B.N. Popov, A generalized cycle life model of rechargeable Li-ion batteries, Electrochim. Acta 51 (10) (2006) 2012–2022.
[44] Y. Hu, S. Yurkovich, Y. Guezennec, B. Yurkovich, Electro-thermal battery model identification for automotive applications, J. Power Sources 196 (1) (2011) 449–457.
[45] A.K. Suttman, Lithium Ion Battery Aging Experiments and Algorithm Development for Life Estimation, Master's thesis, The Ohio State University, 2011.

[6] The CAR Industrial Research Consortium receives funding through annual membership fees paid by: GM, Ford, Cummins, Chrysler, Honda, Oshkosh Truck, Bosch, Eaton, Caterpillar, Lubrizol, Case-New Holland, Renault, Samsung, Tenneco, TRC Inc.